




















# Functional implications of hexameric dynamics in SARS-CoV-2 Nsp15

Manashi Sonowal<sup>1,2</sup>  | Gihan Ketawala<sup>1</sup>  | Nirupa Nagaratnam<sup>1</sup>  |  
 Dhenugen Logeswaran<sup>2</sup>  | Shibom Basu<sup>3</sup>  | Daniele de Sanctis<sup>4</sup>  |  
 Julien Orlans<sup>4</sup>  | Samuel L. Rose<sup>4</sup>  | Rebecca J. Jernigan<sup>1</sup>  | Hao Hu<sup>1,5</sup>  |  
 Jose Domingo Meza Aguilar<sup>1</sup>  | Madurangi E. Ranaweera<sup>1,2</sup>  |  
 Michele A. Zacks<sup>1</sup>  | Julian J.-L. Chen<sup>2</sup>  | Debra T. Hansen<sup>1</sup>  |  
 Lynn G. Schrag<sup>1</sup>  | Raimund Fromme<sup>1,2</sup>  | Sabine Botha<sup>1,5</sup>  |  
 Petra Fromme<sup>1,2</sup> 

<sup>1</sup>Center for Applied Structural Discovery, Biodesign Institute, Arizona State University, Tempe, Arizona, USA

<sup>2</sup>School of Molecular Sciences, Arizona State University, Tempe, Arizona, USA

<sup>3</sup>European Molecular Biology Laboratory (EMBL), Grenoble, France

<sup>4</sup>ESRF, The European Synchrotron, Grenoble, France

<sup>5</sup>Department of Physics, Arizona State University, Tempe, Arizona, USA

## Correspondence

Petra Fromme, Center for Applied Structural Discovery, Biodesign Institute, Arizona State University, Tempe, AZ 85287, USA.  
 Email: [pfromme@asu.edu](mailto:pfromme@asu.edu)

## Funding information

National Science Foundation, Grant/Award Numbers: 1935994, 2031343, 2153503, STC-1231306; Biodesign Center for Applied Structural Discovery

**Review Editor:** Jeanine Amacher

## Abstract

SARS-CoV-2, the virus responsible for the COVID-19 pandemic, has undergone continuous evolution, leading to the emergence of variants with altered transmissibility and immune evasion. For the non-structural proteins (Nsps) of SARS-CoV-2, there are limited structural analyses of their naturally occurring mutations. Here, we identified four non-synonymous single-nucleotide polymorphisms (nsSNPs) in the Epsilon lineage of SARS-CoV-2 within Nsp15, an endoribonuclease critical for immune evasion. Of these Epsilon nsSNPs, E266Q is in the catalytic domain. This study investigates the effects of this on enzymatic activity, structural stability, and oligomeric assembly by serial crystallography. By solving the structure of the Nsp15 hexamer at room temperature of both Nsp15-E266Q and WT in the P2<sub>1</sub> space group to 3 Å, we observed asymmetric motions within its trimer subunits, a feature not visible in previously reported higher-symmetry space groups. These asymmetric motions resemble substrate-induced conformational changes reported in RNA-bound Nsp15 structures, suggesting functional relevance. Biochemical analyses further reveal that Nsp15-E266Q exhibited significantly higher enzymatic activity and thermal stability compared to the wild-type protein. These findings highlight how mutations in Nsp15 contribute to viral replication and immune evasion, offering insights into the molecular mechanisms underlying SARS-CoV-2 variant evolution and potential therapeutic strategies.

## KEYWORDS

asymmetry, E266Q, Epsilon lineage, Nsp15, nsSNP, SARS-CoV-2, space group, X-ray crystallography

## 1 | INTRODUCTION

Severe Acute Respiratory Syndrome Coronavirus 2 (SARS-CoV-2) is responsible for the COVID-19

pandemic, causing significant global morbidity and mortality since its emergence in December 2019 (Machhi et al. 2020). SARS-CoV-2 is an enveloped, positive-sense RNA virus with a non-segmented ~30 kb genome

This is an open access article under the terms of the [Creative Commons Attribution-NonCommercial-NoDerivs](https://creativecommons.org/licenses/by-nc-nd/4.0/) License, which permits use and distribution in any medium, provided the original work is properly cited, the use is non-commercial and no modifications or adaptations are made.  
 © 2025 The Author(s). *Protein Science* published by Wiley Periodicals LLC on behalf of The Protein Society.

(Wu et al. 2020). The genome encodes four structural proteins, several accessory proteins, and two large polyproteins (Pp1a and Pp1ab), which are post-translationally processed into 16 non-structural proteins (Nsps). The Nsps assemble into a large replicase-transcriptase complex (RTC) that performs essential enzymatic and RNA-binding activities necessary for viral replication and infection (Galanopoulos et al. 2020; Kim et al. 2020a). The sequence and function of these Nsps are highly conserved among coronaviruses (Kim et al. 2020b), making them attractive targets for antiviral drug development.

The SARS-CoV-2 genome has continually evolved, accumulating mutations that lead to the emergence of more pathogenic variants. The World Health Organization categorizes these variants based on their transmissibility and immune evasion capabilities into variants of concern (VOC) or variants of interest (VOI). Notable VOCs have included Alpha (B.1.1.7), Beta (B.1.351), Gamma (P.1), Epsilon (B.1.427, B.1.429), Delta (B.1.617.2), and Omicron (B.1.1.529) (Table S1, Supporting Information) each new variant of which showed increased transmissibility and pathogenicity than the original SARS-CoV-2, causing millions of deaths worldwide (CDC 2023). VOIs such as Lambda and Mu have caused less significant impacts. As of September 2023, the U.S. Centers for Disease Control and Prevention (CDC) lists Omicron parent lineages (BA.1 or similar) as VOCs, while other variants such as Alpha, Beta, Gamma, Epsilon, Kappa, Lambda, Eta, Mu, Iota, and Zeta are classified as Variants Being Monitored (VBMs) (CDC 2023).

The Epsilon variant, first detected in California, in July 2020, exhibited increased transmissibility compared to local variants prevalent at the time. The Epsilon variant was initially recognized as a VOC by the CDC. With the emergence of other variants, the impact of Epsilon decreased over time. Epsilon was recognized as a VOI in Feb 2021 and later changed to VBM in September 2021 (CDC 2023). The spike protein of Epsilon harbors four notable non-synonymous single-nucleotide polymorphisms (nsSNPs), S13I, W152C, D614G, and L452R, with D614G being extensively studied in the context of enhanced viral entry (Zhang et al. 2021). The nsSNPs in the non-structural proteins of the Epsilon lineage remain relatively unexplored.

The non-structural protein Nsp15, also known as uridylylate-specific endoribonuclease, plays a crucial role in the viral escape from the host immune system (Hackbart et al. 2020). Nsp15 cleaves the polyuridine sequence of the negative-sense RNA genome of SARS-CoV-2, which otherwise acts as a pathogen-associated molecular pattern (PAMP) recognized by the host's pattern recognition receptor MDA5 (Bhardwaj et al. 2006; Frazier et al. 2021; Hackbart et al. 2020). Nsp15, a 345-residue, 39 kDa protein, consists of three domains: an N-terminal oligomerization domain (amino acids 1–64), a middle domain (amino acids 65–182), and a C-terminal catalytic domain (amino acids 207–347) (Kim et al. 2020b; Pillon

et al. 2021). The enzyme is  $Mn^{2+}$ -dependent and functions as a hexamer, comprising a dimer of trimers. Crystal structures of apo Nsp15 (Jernigan et al. 2023; Kim et al. 2020b) and Nsp15 in complex with inhibitors (Kim et al. 2021) from SARS-CoV-2 have predominantly been solved in a hexagonal space group ( $P6_3$ ), revealing a hexamer composed of two homotrimers based on one monomer of each trimer in the asymmetric unit. Similar hexameric arrangements have been observed in Nsp15 structures from other coronaviruses, such as SARS-CoV (Bhardwaj et al. 2008; Stefano Ricagno et al. 2006), Middle East Respiratory Syndrome-CoV (MERS-CoV) (Zhang et al. 2018), and mouse hepatitis virus (MHV) (Xu et al. 2006). This hexameric organization, reviewed in van Loy et al. (2024), highlights the conserved architecture across coronaviruses. Room-temperature structures of Nsp15 have shown differences in flexibility between the two trimers (Jernigan et al. 2023), an observation confirmed by cryo-EM structures (Pillon et al. 2021). Cryo-EM studies in the presence of single-stranded (ssRNA) and double-stranded RNA (dsRNA) substrates (Frazier et al. 2022a; Ito et al. 2024) have revealed a modest asymmetry within the hexamer induced by substrate binding. While mutational studies across several variants of SARS-CoV-2 have been done (Wilson et al. 2022), comprehensive structural studies on Nsp15 from emerging SARS-CoV-2 variants remain limited.

In this study, we investigate the structural and functional properties of Nsp15 from the Epsilon lineage, focusing on the effects of nsSNPs on enzymatic function. Specifically, we identified a non-synonymous single-nucleotide polymorphism (nsSNP) mutation, E266Q within Nsp15 from Epsilon and characterized its impact on protein expression, enzymatic activity, and structural stability. Furthermore, we determined the structure of Nsp15-E266Q at room temperature by serial millisecond crystallography. In serial millisecond crystallography, X-ray data are collected at Synchrotrons (ESRF) at room temperature in a single X-ray shot mode from millions of microcrystals in a fixed target holder, with 250 single X-ray shots per second. The results reveal an intrinsic asymmetric motion within the hexameric assembly, providing insights into the structural changes and functional impacts of this mutation. Based on these observations, we further re-analyzed the wild-type (WT) crystallographic data from a previous study (Jernigan et al. 2023), and while less pronounced, found the same asymmetric motion within the WT protein of Nsp15.

## 2 | RESULTS

### 2.1 | Identification of non-synonymous SNPs in Nsp15 in the Epsilon lineage

To examine the structural and functional effects of mutations in Nsp15 from the SARS-CoV-2 Epsilon

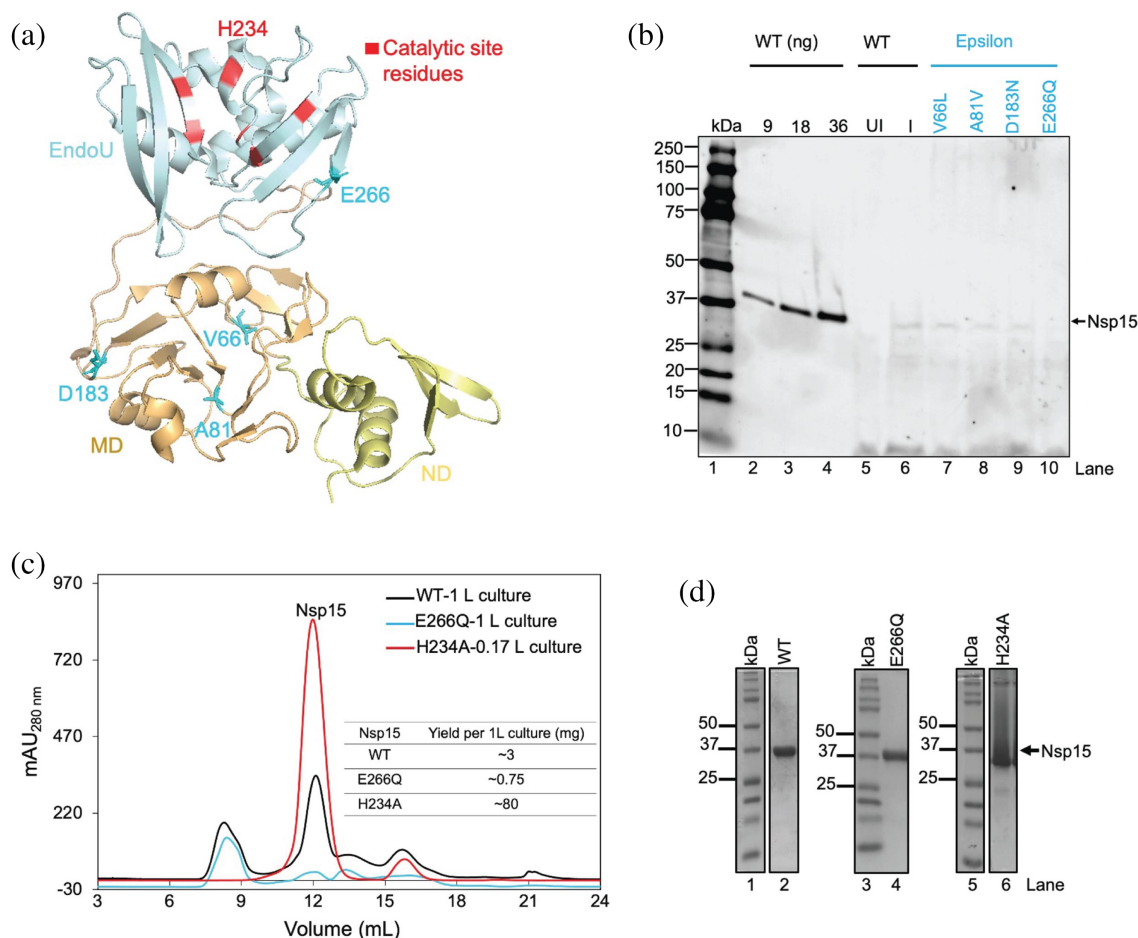


**FIGURE 1** Structural localization of Epsilon Nsp15 nsSNPs and expression and purification of Nsp15 nsSNPs compared to WT. (a) Structural representation of the Nsp15 monomer (PDB entry 7K9P, chain A; Jernigan et al. 2023) highlighting the positions of nsSNPs identified in the Epsilon lineage. Residues altered by nsSNPs are shown in blue, with catalytic residues marked. The catalytic site residue H234A is specifically labeled. (b) Anti-His immunoblot analysis of whole-cell lysates expressing WT and nsSNPs from the Epsilon lineage. Lane 1: protein molecular weight ladder; Lanes 2–4: purified WT loaded at 9, 18, and 36 ng, respectively; Lane 5: uninduced whole-cell lysate of WT; Lane 6: IPTG-induced whole-cell lysate of WT; Lanes 7–10: IPTG-induced whole-cell lysates containing Epsilon lineage nsSNPs. (c) Size exclusion chromatography (SEC) profiles comparing protein elution from WT (black, 1 L culture), Nsp15-E266Q (blue, 1 L culture), and H234A (red, 0.17 L culture). Protein yields (mg per 1 L culture) are indicated. (d) Coomassie-stained SDS-PAGE gels of purified Nsp15 corresponding to the SEC peaks in (c), confirming protein purity. Lanes 1, 3, 5: protein molecular weight ladder; Lane 2: WT; Lane 4: Nsp15-E266Q; Lane 6: H234A.

lineage, we performed a genome sequence alignment between the Epsilon variants and the original Wuhan SARS-CoV-2 strain. From this alignment, we extracted the sequence region corresponding to Nsp15. This analysis identified four non-synonymous single-nucleotide polymorphisms (nsSNPs) leading to amino acid substitutions: V66L, A81V, D183N, and E266Q. Structural mapping of these mutations (Figure 1a) revealed that V66L, A81V, and D183N are situated within the middle domain, while E266Q is located within the catalytic domain and has been previously implicated in directly interacting with adjacent monomers (Bhardwaj et al. 2008).

The catalytic domain of Nsp15 is essential for its endoribonuclease activity, which facilitates immune evasion by cleaving polyuridine sequences in viral RNA

(Frazier et al. 2021; Hackbart et al. 2020). The presence of E266Q within this domain suggests the potential for altered enzymatic activity due to local structural changes or disrupted interactions critical for catalysis.

## 2.2 | Expression studies of Nsp15-E266Q suggest auto-inhibitory activity

To evaluate the expression of all nsSNPs from Epsilon, we used *Escherichia coli* for recombinant protein production. Expression levels were analyzed from whole cell lysates and visualized by anti-His Western blot. Purified WT protein from original SARS-CoV-2 was loaded in three different quantities (9 ng, 18 ng, 36 ng)

as a reference (Figure 1b, lanes 2–4). We observed that Nsp15-E266Q exhibited significantly lower expression levels (Figure 1b, lane 10) compared to wild-type (WT) (Figure 1b, lane 6), as indicated by weak bands in the anti-His Western blot.

Considering the reduced expression of Nsp15-E266Q compared to WT, we performed a comparative analysis of protein purification yields. To enable this comparison, we included the catalytically inactive H234A mutant, which has been previously characterized both in SARS-CoV (Guarino et al. 2005) and SARS-CoV-2 (Guarino et al. 2005; Otter et al. 2024). This active site mutation allows Nsp15 to bind to RNA substrates while eliminating its ability to cleave them, making it a valuable control for experiments involving Nsp15-E266Q and WT. Notably, previous studies have shown that H234A expresses at higher levels than WT in both SARS-CoV (Guarino et al. 2005) and SARS-CoV-2 (Otter et al. 2024). Consistent with these reports, our data showed that H234A exhibited very high amount of purified Nsp15 hexamer. Following Ni-NTA affinity chromatography, size exclusion chromatography (SEC) profiles showed a purification yield of approximately 80 mg per liter of culture for H234A, compared to ~3 mg per liter for WT and 0.75 mg for Nsp15-E266Q, as quantified using a Nano-drop spectrophotometer (Figure 1c). SDS-PAGE analysis of the SEC peaks of purified Nsp15 (Figure 1c) showed distinct bands corresponding to the expected molecular weight of Nsp15 (42 kDa) for all three proteins (Figure 1d). Further analysis of SEC fractions from both WT and Nsp15-E266Q revealed similar protein distribution across chromatographic peaks (Figure S1a–d), suggesting that the E266Q mutation does not significantly alter the oligomeric state of Nsp15. These observations indicate that while Nsp15-E266Q can be expressed and purified, its recombinant yield is significantly lower than that of WT and the H234A mutant.

## 2.3 | Nsp15-E266Q exhibits enhanced catalytic activity compared to wild-type

Given that the E266Q mutation is located within the catalytic domain of Nsp15, we hypothesized that this nsSNP could influence the enzyme's catalytic activity. To investigate this, we used a previously established assay used for WT (PDB entry: 7K9P) activity evaluation using a 21-nucleotide RNA substrate, (Jernigan et al. 2023) labeled at the 3' terminus with a fluorophore (Figure 2a). To test whether the E266Q mutation drastically influences Nsp15 catalytic activity, we performed the *in vitro* assay. Both Nsp15-E266Q and WT could cleave the RNA substrate, generating fragments of the expected size (Figure 2b, lanes 3 and 4). As expected, the catalytically inactive mutant H234A and the buffer

control showed no detectable cleavage activity (Figure 2b, lanes 1 and 2).

To further quantify and characterize the catalytic behavior of Nsp15-E266Q, we conducted fluorescence-based kinetic assays using a fluorogenic RNA oligonucleotide, 6-FAM-5'dArUdAdA3'-6-TAMRA. This substrate contained a fluorophore (6-carboxyfluorescein, FAM) at the 5'-terminus and a quencher (6-carboxytetramethylrhodamine, TAMRA) at the 3'-terminus, enabling high precision and sensitivity in monitoring of product synthesis. These assays revealed that Nsp15-E266Q exhibited an increase in activity compared to WT (Figure 2c). Additionally, kinetic parameters were determined, with the maximum velocity ( $V_{max}$ ) and Michaelis constant ( $K_m$ ) calculated at 8720 RFU/min and 1.37  $\mu$ M for Nsp15-E266Q and 6144.6 RFU/min and 1.57  $\mu$ M for WT (Figure 2d).

## 2.4 | Nsp15-E266Q shows enhanced thermostability compared to wild-type

To investigate whether the observed differences in catalytic activity were linked to changes in the structural stability of Nsp15, we performed differential scanning fluorimetry (Figure 2e). Nsp15-E266Q, H234A, and WT were analyzed over a temperature range of 30–95°C. Consistent with prior studies on WT (Choi et al. 2021; Kim et al. 2020b) two distinct thermal transition temperatures ( $T_m$ ) were observed: an initial transition at approximately 45°C, likely corresponding to hexamer dissociation (Kim et al. 2020b), and a second transition at around 58°C, corresponding to monomer unfolding (Kim et al. 2020b). Interestingly, Nsp15-E266Q exhibited a slight increase in thermal stability compared to WT and H234A, with its  $T_m$  values for the first (1st  $T_m$ ) and second (2nd  $T_m$ ) transitions measured at 46.5 and 60.5°C, respectively. In contrast, WT and H234A showed  $T_m$  values of approximately 44–46°C and 58.5°C for the first and second transitions. These results indicate that the E266Q mutation enhances the thermostability of Nsp15 relative to both WT and the catalytically inactive H234A mutant.

## 2.5 | Nsp15-E266Q crystal structure in the P6<sub>3</sub> space group

To investigate potential structural changes caused by the E266Q mutation, which could explain its increased enzymatic activity and thermal stability, we determined the crystal structure of Nsp15-E266Q using serial X-ray crystallography. Purified Nsp15-E266Q was crystallized using the batch crystallization method, producing needle-like crystals of approximately 50–100  $\mu$ m long (Figure S2 a). Five microliter of the suspension of the crystals was loaded on a fixed target holder using a foil-



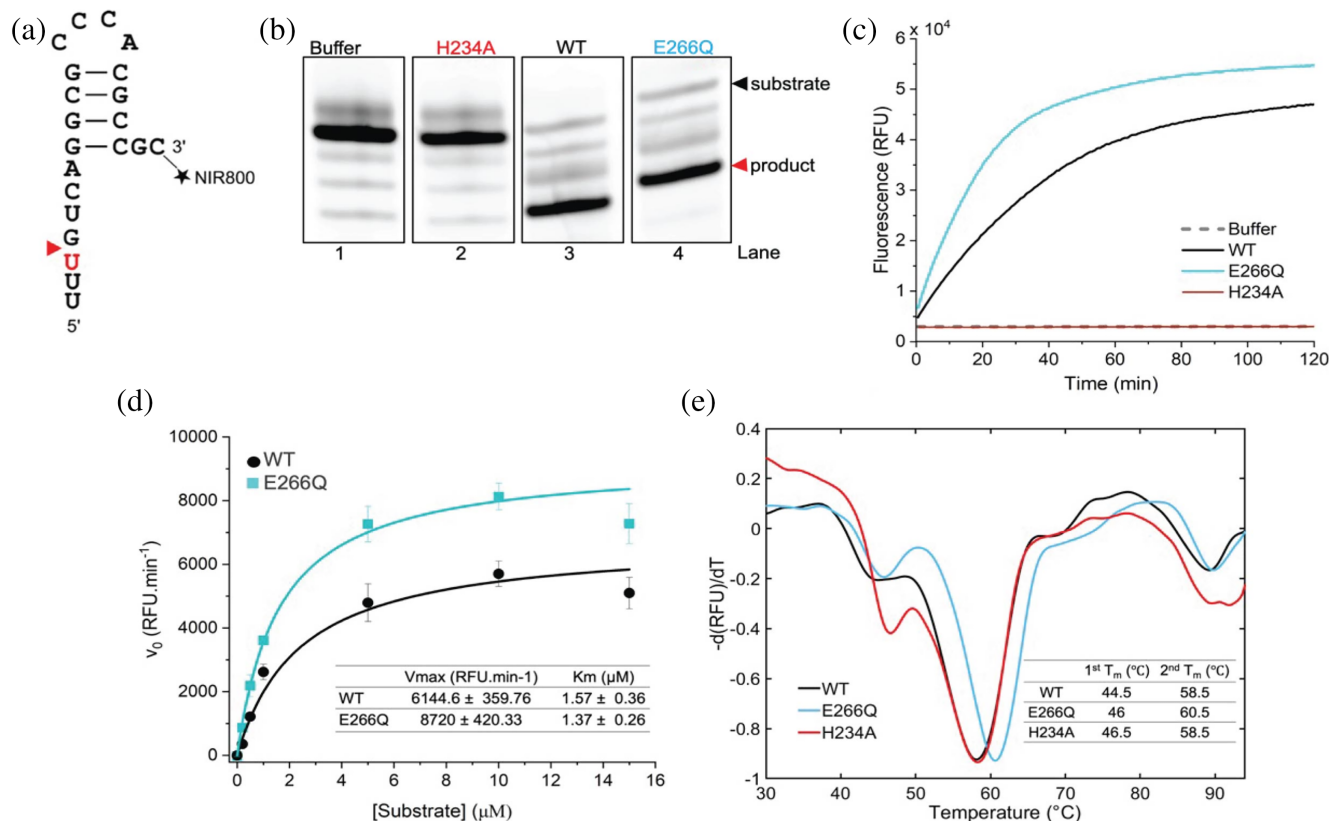


**FIGURE 2** Functional activity, enzymatic kinetics, and thermal stability of Nsp15 variants. (a) 21 nucleotide (nt) RNA substrate labeled with a NIR-800 (Near Infra-Red 800nm) fluorophore at the 3'-end. The red triangle indicates the cleavage site between U and G, resulting in an 18 nt product. (b) Urea-PAGE gel-based functional assay performed using the RNA substrate shown in (a). Lane 1: SEC buffer (no enzyme control); Lane 2: catalytically inactive mutant H234A; Lane 3: WT; Lane 4: Nsp15-E266Q. (c) Fluorescence-based kinetic assay performed with the fluorogenic RNA substrate 6-FAM-5'-dArUdAdA3'-6-TAMRA. A control reaction without enzyme is shown in dash lines. (d) Michaelis-Menten plots for WT and Nsp15-E266Q, showing differences in kinetic parameters ( $V_{max}$  and  $K_m$ ). Errors represent the standard deviation of triplicates. (e) Thermal stability analysis of WT, Nsp15-E266Q, and H234A using first derivative plots of relative fluorescence versus temperature. Transition temperatures for the first (1st  $T_m$ ) and second (2nd  $T_m$ ) thermal unfolding stages are indicated.

on-foil fixed-target delivery system. Data was collected at the ID-29 beamline at the European Synchrotron Radiation Facility (ESRF). X-ray data collection was performed in a single-shot mode at room temperature where diffraction data from the crystals were collected with 250, 90 μs long X-ray shots/second using a chopper. The chip was automatically moved by 50 μm between the X-ray shots. Data collection of 40,000 images/chip was performed in 8 min/chip (Doak et al. 2024). The data set consists of 54,091 indexed images and the structure was resolved to a resolution of 3 Å (Table 1 and Figure S2 b).

Nsp15 is known to form a hexamer comprising two homotrimers, with flexibility differences between the trimers (Jernigan et al. 2023). As previous crystallographic studies of Nsp15 were conducted in the  $P6_3$  space group with each asymmetric unit containing one monomer from each trimer (Jernigan et al. 2023; Kim et al. 2020b; Kim et al. 2021), we initially solved the Nsp15-E266Q structure in this space group (Figure S2 b). Comparison with a previous study of the room temperature WT structure, which was solved by serial

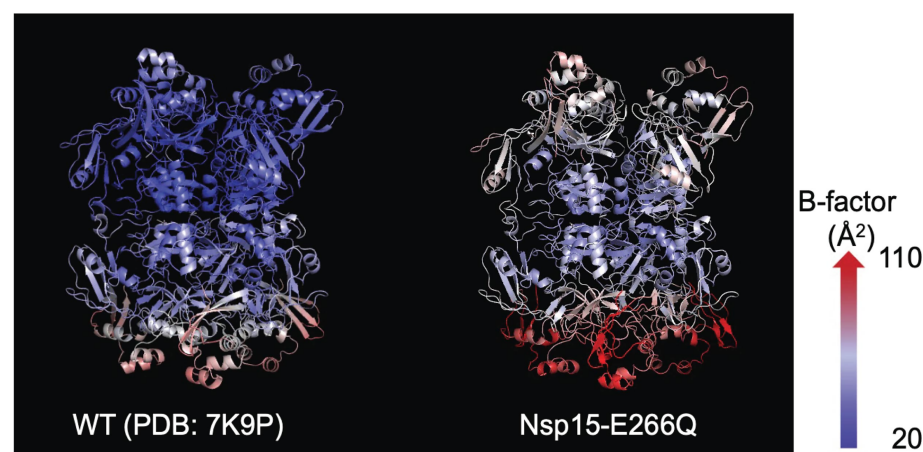
X-ray crystallography using an X-ray free-electron laser (XFEL) (PDB entry 7K9P; Jernigan et al. 2023), showed high structural similarity, with a root-mean-square deviation (RMSD) for  $C\alpha$  of 0.98 Å. Despite the conserved overall configuration, Nsp15-E266Q (Figure 3, right) exhibited higher overall B-factors compared to WT (Figure 3, left), suggesting increased flexibility in the mutant structure.

## 2.6 | Nsp15-E266Q structure in the $P2_1$ space group revealed asymmetric motion

To better understand the higher B-factors observed in Nsp15-E266Q and explore potential structural asymmetry, we solved its structure in the  $P2_1$  space group at 3 Å resolution (Table 1). For comparison, we also solved the WT structure (PDB entry 7K9P) in the same space group ( $P2_1$ ). Unlike structures in the  $P6_3$  space group, which contain one monomer from each trimer in the asymmetric unit (Jernigan et al. 2023; Kim et al. 2020b; Kim et al. 2021), the  $P2_1$  space group

**TABLE 1** Data processing and refinement statistics.

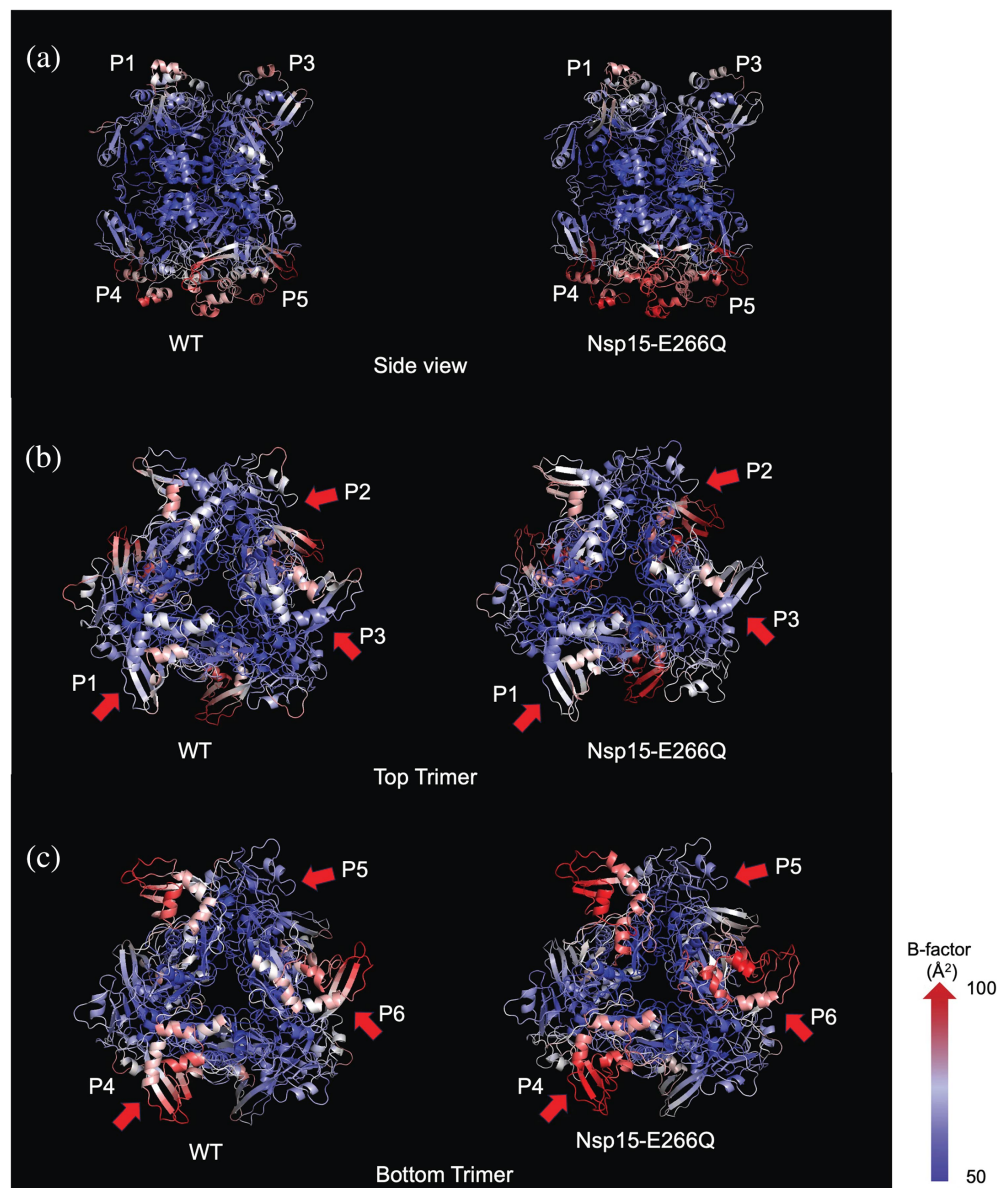
Data processing			
Structure	Nsp15-E266Q in P6 <sub>3</sub>	Nsp15-E266Q in P2 <sub>1</sub>	WT (7K9P) in P2 <sub>1</sub>
Wavelength (Å)	1.072	1.072	1.278
Space group	P6 <sub>3</sub>	P2 <sub>1</sub>	P2 <sub>1</sub>
No. of indexed patterns	54,091	55,068	26,081
Unit cell a, b, c (Å)	154.2, 154.2, 116.2	154.7, 116.6, 154.8	153.4116.9, 153.4
	90, 90, 120	90, 119.4, 90	90°, 119.8°, 90°
Resolution (Å)	30–3.0 (3.11–3.0)	30–3.0 (3.11–3.0)	20–3.0 (3.11–3.0)
No. of unique reflections	31,487 (3119)	96,013 (4736)	95,567 (9456)
Redundancy	420.85 (292.6)	280.16 (196.4)	83.32 (58)
SNR	6.8 (1.3)	3.6 (0.9)	2.70 (0.8)
Completeness (%)	100 (100)	100 (100)	100 (100)
CC*	0.99 (0.65)	0.98 (0.38)	0.97 (0.3)
CC1/2	0.98 (0.27)	0.93 (0.08)	0.89 (0.04)
Refinement			
R <sub>work</sub>	0.17	0.18	0.20
R <sub>free</sub>	0.19	0.20	0.22
Mean isotropic B-factor (Å <sup>2</sup> )	82.0	76.0	73.0
Wilson plot B-factor (Å <sup>2</sup> )	80.2	86.0	85.5
No. of atoms			
Protein	5,492	16,476	16,476
Solvent	0	0	0
RMSD, bond lengths (Å)	0.008	0.008	0.008
RMSD, bond angles (°)	1.11	0.45	0.45
Ramachandran plot (%)			
Favored	97	93	94
Allowed	3	6	5
Outliers	0	1	0.53
PDB ID	9MRW	9MRU	9MRY

**FIGURE 3** Comparison of B-factors between WT Nsp15 (PDB entry 7K9P) and Nsp15-E266Q solved in P6<sub>3</sub>. Cartoon representation of Nsp15 structures showing B-factors for WT (PDB entry 7K9P, left; Jernigan et al. 2023) and Nsp15-E266Q (right). Regions with the lowest B-factors (indicating the least flexibility) are shown in blue, while regions with the highest B-factors (indicating the greatest flexibility) are shown in red. The color gradient spans from 20 Å<sup>2</sup> (dark blue) to 110 Å<sup>2</sup> (dark red).

contains a full hexamer in the asymmetric unit, minimizing potential symmetry biases. This analysis revealed that both trimers of the hexamer are indeed intrinsically asymmetric within themselves as it pertains to B-factors. Consistent with prior observations, one trimer

displayed higher B-factors overall, indicating greater flexibility. Additionally, Nsp15-E266Q had slightly higher overall B-factors compared to WT. We have therefore assigned each monomer a unique label with P1, P2, and P3 making up the less flexible trimer, and

**FIGURE 4** Structures of WT and Nsp15-E266Q solved in the  $P2_1$  space group reveal changes in asymmetric motion. (a) Side-views of WT (left) and Nsp15-E266Q (right) structures are shown colored by B-factor, highlighting the variability in B-factors across the hexamer and within the trimers making up the trimers. The monomers are labeled from P1 to P6. (b) Top views of WT (left) and Nsp15-E266Q (right) of the top trimer. The differences in flexibility regions are shown with red arrows. (c) Top views WT (left) and Nsp15-E266Q (right) of the bottom trimer. The color gradient spans from 50  $\text{\AA}^2$  (dark blue) to 100  $\text{\AA}^2$  (dark red).



P4, P5, and P6 the second, more flexible trimer (Figure 4a). Within the top, less flexible trimer, one monomer (P2) had higher B-factors compared to the other two monomers (P1 and P3) (Figure 4b). Similarly, in the more flexible trimer, one monomer (P6) showed higher B-factors compared to the other two monomers (P4 and P5) (Figure 4c). This asymmetric motion within each trimer was also independently identified from cryo-electron microscopy (Cryo-EM) studies of Nsp15 bound to RNA (Frazier et al. 2022b; Ito et al. 2024). These published studies revealed several key attributes of Nsp15 substrate binding: First, the substrate interacts asymmetrically with two monomers from one trimer and extends to contact a monomer from the second trimer. Second, the substrate binding induces very little inter-monomer asymmetry. Third, the monomer local resolution, a proxy for dynamics in cryo-EM, is consistent with our observations of Nsp15-E266Q in

the  $P2_1$  space group. Interestingly, the degree of asymmetric motion within the trimers was more pronounced in Nsp15-E266Q compared to WT, highlighting a structural feature potentially linked to the mutation's enhanced catalytic activity and thermal stability. This level of detail could not be observed in previous crystallographic structures of Nsp15 solved in the  $P6_3$  space group, highlighting the importance of structural investigations at lower symmetry.

### 3 | DISCUSSION

In this study, we investigated the functional and structural properties of the E266Q mutation, a mutation in the catalytic domain of Nsp15 from the SARS-CoV-2 Epsilon lineage, for its potential role in enhanced virulence. Nsp15-E266Q exhibits significantly higher

enzymatic activity than the wild-type (WT) protein, as shown by endpoint cleavage assays and fluorescence kinetics, which may enhance viral replication and host cell manipulation, contributing to the increased transmissibility of the Epsilon lineage. However, Nsp15-E266Q displayed reduced expression levels and purification yields, likely due to cleavage of its own mRNA during translation. Thermal stability analysis showed that Nsp15-E266Q has a slightly higher thermal transition temperature ( $T_m$ ) than WT, suggesting it is more stable.

To evaluate the conservation of residue E266 across coronaviruses, we performed a multiple sequence alignment of Nsp15 from SARS-CoV-2, SARS-CoV, MERS-CoV, MHV, and HCoV-229E. The alignment revealed that while the E266Q mutation is specific to the SARS-CoV-2 Epsilon lineage, the equivalent position in MHV contains a glutamine (Q), suggesting potential functional similarities between these proteins (Figure S3). This observation may indicate a conserved role of glutamine at this position in certain coronaviruses, which could have structural or catalytic implications.

Mutations in Nsp15's catalytic domain often affect enzymatic activity and structural stability, as this region is critical for maintaining the integrity of the catalytic domain, EndoU fold (Wilson et al. 2022). The E266Q mutation itself is located on the far side of one of the antiparallel  $\beta$ -sheets that compose the catalytic pocket directly opposite of the active site residue K289. Previous structural studies of E266A in SARS-CoV show that the residue makes a direct inter-monomeric salt-bridge with R61, which has been shown to be critical for oligomerization (Bhardwaj et al. 2008). While the E266A mutation disrupted oligomerization in SARS-CoV, we observed no such changes in SARS-CoV-2 Nsp15. This suggests that E266 serves a rheostatic role in SARS-CoV-2. The attenuation of the inter-monomeric salt bridge between E266 and R61 in Nsp15-E266Q led to greater movement in the enzymatic domain, which in turn likely enhances catalytic turnover. This added motility may also facilitate functional conformational changes necessary for enhanced catalytic activity. Therefore, the observed increase in both stability and activity can be understood in terms of stabilizing an active form of the enzyme, while greater conformational flexibility enhances catalytic efficiency. However, higher-resolution structural studies and functional analyses with RNA substrates are needed to clarify these effects.

Interestingly, the increased thermal stability and enzymatic activity of E266Q suggest a potential advantage in viral replication. Nsp15 is known to play a role in evading the host immune response by degrading viral RNA intermediates even earlier than could otherwise trigger innate immune sensors. In addition, there is a slight shift in the hexamer transition peak in Nsp15-E266Q as

compared to WT (Figure 2e), suggesting that the Nsp15-E266Q hexamer is more robust to temperature increases. This could help the virus better withstand the host fever response, potentially leading to higher infectivity. While E266Q exhibits enhanced enzymatic and stability properties, the observed variations in expression levels make it challenging to attribute these effects solely to the mutation. Future studies normalizing Nsp15 expression in recombinant systems or viral constructs will be necessary to determine whether these biochemical differences translate into increased viral fitness. Further studies are needed to establish a direct connection between the enhanced biochemical properties of E266Q and its role in viral pathogenesis. Performing viral replication assays in cell culture models could help determine whether this mutation confers a replicative advantage. Additionally, in vivo infection studies could provide insights into immune evasion mechanisms. Structural analysis of the E266Q mutant in complex with its RNA substrate may also reveal mechanistic changes contributing to its altered activity.

Previous X-ray crystallography studies of Nsp15 analyzed in  $P6_3$  space group, from both our group and others (Jernigan et al. 2023; Kim et al. 2020b), have robustly shown steric symmetry across the dimeric interface while displaying prominent asymmetry in B-factors. However, our findings revealed inherent asymmetric motion in both WT and E266Q Nsp15 hexamers, a feature previously obscured in crystallographic studies due to over-predicted symmetry. Recent cryo-EM studies demonstrated that only one monomer per trimer binds dsRNA substrates (Figure 5) (Frazier et al. 2022a; Ito et al. 2024). Reprocessing our data in a lower-symmetry space group revealed significant asymmetry in monomer flexibility, particularly pronounced in the E266Q mutant compared to the WT protein. This asymmetry may therefore be crucial for the protein's catalytic mechanism and likely contributes to enhanced enzymatic activity as observed in our biochemical studies.

In summary, the E266Q natural variant of Nsp15 underscores the intricate balance between enzymatic activity, structural stability, and expression efficiency in viral proteins. These findings provide valuable insights into the molecular mechanisms driving SARS-CoV-2 evolution, with implications for developing targeted therapeutic strategies against the Epsilon lineage and other emerging strains.

## 4 | METHODS

### 4.1 | Bioinformatic analysis

A total of 126 genomes specific to the SARS-CoV-2 Epsilon lineage were downloaded from the GISAID (Global Initiative on Sharing Avian Influenza Data)



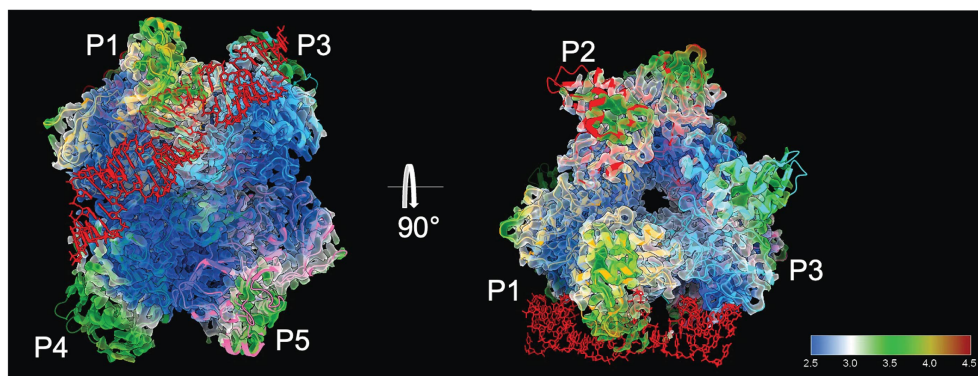


**FIGURE 5** Cryo-EM structure of Nsp15-dsRNA (8UD3) complex. Analysis of the Nsp15-RNA complex maps (EMD-42145, consensus) reveals double-stranded RNA binding primarily within the top trimer (monomers P1 and P3) and extending to interact with the bottom trimer (monomer P4), as reported by Ito et al. (2024). Local resolution analysis at a contour level of 0.35 supports the relative completeness of P1 to <3.5 Å, including loops, while all other loops in the monomers are unsupported.

database (Shu and McCauley 2017). These genomes were aligned with the original Wuhan reference genome using Sequencer 5.4.6. The region specific for Nsp15 (Wuhan reference coordinates 19,621–20,658) was analyzed to identify single-nucleotide polymorphisms (SNPs). The SNPs leading to amino acid changes (nsSNPs) in the Nsp15 protein were retrieved. A schematic is shown in Figure S4.

## 4.2 | Expression plasmids

The expressed Nsp15 proteins were designed with an N-terminal TEV (tobacco etch virus) cleavable hexahistidine tag. WT was expressed from plasmid pHis-TEV-Nsp15 (Jernigan et al. 2023). The expression plasmids generated in this study are listed in Table S2 and were purchased from GenScript. The plasmid DNA sequences are identical to pHis-TEV-Nsp15 except for the codon changes in Table S2. For plasmid pHis-TEV-Nsp15-E266Q, Figures S5 a–c show the vector map, complete DNA sequence, and expressed protein sequence, respectively. Plasmids and their sequences are available from Addgene (Table S2).

## 4.3 | Protein expression and purification

WT and Epsilon Nsp15 nsSNPs were expressed and purified following previously established protocols (Jernigan et al. 2023). Full gels are provided in Figure S6 a,b.

## 4.4 | RNA substrate functional and kinetic assays

The RNA substrate for functional assays was described previously (Jernigan et al. 2023). An RNA substrate

with NIR-800 (Near Infra-Red 800nm) fluorophore label at the 3' end was synthesized (Integrated DNA Technologies). RNA oligos were dissolved at 100  $\mu$ M in nuclease-free water and then diluted to 5  $\mu$ M for the functional assay with nuclease-free water.

Assays were performed in 50 mM Tris-HCl pH 7.5, 50 mM KCl, and 1 mM DTT unless stated otherwise. For functional assay, reactions used 1.2  $\mu$ M of enzyme, 1  $\mu$ M RNA substrate, and 5 mM  $MnCl_2$ . Reaction mixtures were incubated for 15 min at 25°C before terminating with an equal volume of 2 $\times$  urea loading dye (8M urea, 20 mM Tris-HCl pH 7.5, 1 mM EDTA, 0.05% (w/v) xylene cyanol and 0.05% (w/v) bromophenol blue). Prior to urea-PAGE, reactions were incubated at 95°C for 2 min. Products were separated by electrophoresis on 10% or 15% urea-PAGE. Gels were imaged on an ImageQuant 800. Full gel is provided in Figure S6c.

For kinetic assays, fluorogenic RNA oligonucleotide substrate 5'6-FAM-dArUdAdA-6-TAMRA3' was purchased from GenScript. Assays were performed with 50 nM Nsp15, and 0.25  $\mu$ M substrate, supplemented with 5 mM  $MnCl_2$  for 2 h at 25°C and monitored using FAM filters in a Stratagene Mx3005P real-time PCR system (Agilent Technologies). For  $K_m$  and  $V_{max}$ , assays were performed with substrate concentration ranging from 0 to 15  $\mu$ M. Initial velocities were calculated with initial differences in relative fluorescence and time. All reactions were performed in triplicates, and the data was averaged, plotted, and analyzed using OriginPro 2024b.

## 4.5 | Differential scanning fluorimetry

Differential Scanning Fluorimetry was performed according to Kim et al. (2020b). Briefly, 10  $\mu$ M Nsp15 in SEC buffer was incubated with 5X SYPRO Orange for 30 min on ice. A 50  $\mu$ L sample was then loaded in a

96-well plate on Vii6 life real-time PCR system. Acquisition of fluorescence signal was performed from 20 to 95°C with a temperature ramp rate of 1°C/60 s.

## 4.6 | Protein crystallization

Nsp15 crystals were obtained using the batch method with agitation, following previously described protocols (Jernigan et al. 2023) with slight modifications. Purified Nsp15 protein in SEC buffer was concentrated to 15–20 mg/mL (Amicon Ultra-0.5 mL centrifugal filters with a 30 kDa MWCO) at 7000*g* and 12°C. The precipitant solution containing 100 mM HEPES-NaOH, pH 7.5, 200 mM calcium acetate, and 8% (w/v) PEG 8000 was then rapidly mixed with the concentrated protein solution on ice in a 1:6 (protein: precipitant) volume ratio. Crystals were allowed to grow at 4°C.

## 4.7 | X-ray diffraction data collection

### 4.7.1 | Experimental setup

Diffraction data for Nsp15-E266Q were collected on the ID29 beamline at the European Synchrotron Radiation Facility (ESRF). Data were acquired using an X-ray energy of 11.56 keV with 4 µm × 2 µm beam size and exposure of 90 µs at a repetition rate of 231.25 Hz. The beam transmission was set to 40%, providing an average photon flux of  $1.44 \times 10^{11}$  photons per exposure. The Jungfrau detector was placed 150 mm from the samples to capture scattered X-rays. A custom small foil fixed-target delivery system developed at ESRF (Doak et al. 2024) was utilized, which helped in reducing sample consumption. This system consisted of two mylar films with a thickness of 13 µm. Approximately 3 µL of dense crystal slurry was loaded and sealed in between two mylar films, as described in Orlans et al. (2025). For data collection, the foil was continuously scanned by X-ray pulses at 231.25 Hz repetition rate with 20 µm spacing between two consecutive shots.

## 4.8 | Data processing

### 4.8.1 | Processing Nsp15-E266Q data set with P6<sub>3</sub> space group (Nsp15-E266Q-P6<sub>3</sub>)

The dataset obtained from ESRF consisted of 48,079 crystal hits, which were identified using peakfinder8 within the CrystFEL software suite (version 11.1) (White et al. 2012). Key parameters for hit finding included a threshold of 800, a minimum of 10 peaks/image, a signal-to-noise ratio (SNR) of 5.5, pixel count limits ranging from 4 to 20 pixels/peak, a minimum

resolution (in pixels) of 60, a maximum resolution of 900, and integration radii of 3, 5, and 7 pixels. Of the 48,079 hits, 55,068 crystals (114.53%) were successfully indexed (with a hexagonal target cell), with some patterns reflecting contributions from multiple crystal lattices. The multi-flag was used to detect and resolve multi-lattice diffraction patterns, ensuring that all contributions from overlapping crystals in a single frame were accurately indexed.

The indexing process involved a combination of algorithms, including MOSFLM (Powell 1999), XDS (Kabsch 2010), Xgandalf (Gevorkov et al. 2019), Dirax (Duisenberg 1992), ASDf (White 2019), and TakeTwo (Ginn et al. 2016). Indexing tolerances were set at 10 for cell axes and 3.5 for inter-axial angles. The E266Q-P6<sub>3</sub> dataset exhibits indexing ambiguity. Thus, the indexed diffraction intensities were processed using AMBIGATOR (Brehm and Diederichs 2014) (part of the CrystFEL package) with the re-indexing operator: -h,k,-l.

### 4.8.2 | Processing Nsp15-E266Q data set with P2<sub>1</sub> space group (Nsp15-E266Q-P2<sub>1</sub>)

The same hit-finding and indexing parameters used for Nsp15-E266Q in the P6<sub>3</sub> space group were employed for this analysis. Data processing was carried out using CrystFEL version 11.1 (White et al. 2012). A total of 48,081 hits were identified, and from these, 54,091 crystals were successfully indexed using a monoclinic target cell for Nsp15-E266Q.

### 4.8.3 | Reprocessing WT dataset with P2<sub>1</sub> space group (WT-P2<sub>1</sub>)

This experiment was conducted as part of the RAPID ACCESS X-Ray Free Electron Beamtime campaign during the COVID-19 pandemic (Beamtime P172 and P182). Jernigan et al. described the sample delivery and data collection process in detail (Jernigan et al. 2023). For hit-finding, Peakfinder8 in the CrystFEL software suite (version 11.1) was used with the following parameters: -threshold = 100 -min-snr = 5 -min-pix-count = 1 -min-res = 80 and -max-res = 300. Diffraction patterns with more than 10 peaks were classified as hits. 29,674 hits were found, and of those hits, 26,081 crystals were indexed with the combined use of the indexing algorithms including MOSFLM (Powell 1999), XDS (Kabsch 2010), Xgandalf (Gevorkov et al. 2019), Dirax (Duisenberg 1992), ASDf (White 2019), and TakeTwo (Ginn et al. 2016). The target unit cell was a monoclinic unit cell with Indexing tolerances set at 10 for cell axes and 3.5 for inter-axial angles.

#### 4.8.4 | Merging and converting to CCP4-compatible format

The reflection intensities were then merged and integrated in accordance with the respective point group for each dataset with PARTIALATOR (also from the CrystFEL package), employing one iteration and the unity model. Next, the merged intensities were converted into CCP4-compatible mtz format (Brehm and Diederichs 2014) using a wrapper script, create-xscale, followed by XDSCONV (Kabsch 2010).

#### 4.9 | Refinement

The scaled datasets were processed using the AIMLESS (Evans and Murshudov 2013) program. For molecular replacement, the MOLREP (Vagin and Teplyakov 1997) program from the CCP4 (Agirre et al. 2023) software package utilized the crystal structure of Nsp15, specifically PDB entry 7K9P, as the search model. Modifications to the search model included the removal of all water molecules and ligands (citrate). Additionally, one chain was removed from the originally two-chained model, and all B-factors were reset to 30 Å<sup>2</sup> to minimize the bias introduced by the model. The subsequent refinement was performed using REFMAC5 (Murshudov et al. 2011), Phenix.refine (Afonine et al. 2012), and manually through Coot (Emsley et al. 2010). Finally, the model underwent a final refinement cycle with the PDB-redo pipeline (Joosten et al. 2014; van Beusekom et al. 2018) prior to submission. The figures were produced using PyMOL (Schrödinger, LLC) (Schrodinger, LLC 2015).

#### AUTHOR CONTRIBUTIONS

**Manashi Sonowal:** Conceptualization; formal analysis; investigation; methodology; validation; writing – original draft. **Gihan Ketawala:** Data curation; formal analysis; software; visualization; writing – original draft. **Nirupa Nagaratnam:** Conceptualization; formal analysis; investigation; methodology. **Dhenugen Logeswaran:** Investigation; methodology; writing – review and editing. **Shibom Basu:** Investigation; writing – review and editing. **Daniele de Sanctis:** Investigation; writing – review and editing. **Julien Orlans:** Investigation. **Samuel L. Rose:** Investigation. **Rebecca J. Jernigan:** Investigation. **Hao Hu:** Investigation. **Jose Domingo Meza Aguilar:** Investigation. **Madurangi E. Ranaweera:** Investigation. **Michele A. Zacks:** Funding acquisition. **Julian J.-L. Chen:** Resources. **Debra T. Hansen:** Methodology; writing – review and editing. **Lynn G. Schrag:** Validation; visualization; supervision; writing – review and editing. **Raimund Fromme:** Conceptualization; project administration; investigation; formal analysis; software. **Sabine Botha:** Conceptualization; data curation; formal analysis; methodology;

software; validation; writing – review and editing; writing – original draft. **Petra Fromme:** Conceptualization; funding acquisition; project administration; resources; supervision; validation; writing – review and editing; investigation.

#### ACKNOWLEDGMENTS

We would like to thank the staff of ESRF and EMBL Grenoble for assistance and support in using the beamline ID29 under proposal number MX-2546. We would further like to thank Xiaojiang S Chen and Fumiaki Ito for providing access to their cryo-EM maps. We would also like to thank Dr. Dalton Kiefer and the Biodesign Institute's shared facility for supporting DSF experiments and Deeksha Satyabola for facilitating access to equipment for enzyme kinetic assays. This work was supported by the National Science Foundation's Science and Technology Center "BioXFEL" through award STC-1231306, RAPID grant award "IIBR: Instrumentation: Time-resolved studies of the SARRS-CoV-2 endonuclease Nsp15" (award 2031343) and the Biodesign Center for Applied Structural Discovery at Arizona State University. Petra Fromme and Sabine Botha further acknowledge support by the National Science Foundation Bio Directorate under midscale research infrastructure Grants 2153503 and 1935994.

#### CONFLICT OF INTEREST STATEMENT

The authors declare no conflicts of interest.

#### DATA AVAILABILITY STATEMENT

Atomic coordinates and structure factors were deposited to Protein Data bank (PDB) under the accession codes: Nsp15-E266Q-P2<sub>1</sub> (9MRU), Nsp15-E266Q-P6<sub>3</sub> (9MRY), WT-P2<sub>1</sub> (9MRW). DOI of the dataset will be provided, and the data will be publicly available.

#### ORCID


Manashi Sonowal  <https://orcid.org/0000-0002-4665-8831>

Gihan Ketawala  <https://orcid.org/0000-0002-9436-3536>


Nirupa Nagaratnam  <https://orcid.org/0000-0002-3201-930X>

Dhenugen Logeswaran  <https://orcid.org/0000-0002-3522-3883>

Shibom Basu  <https://orcid.org/0000-0001-6484-8236>

Daniele de Sanctis  <https://orcid.org/0000-0003-0391-8290>

Julien Orlans  <https://orcid.org/0000-0002-6933-2287>








Samuel L. Rose  <https://orcid.org/0000-0003-4824-4066>

Rebecca J. Jernigan  <https://orcid.org/0000-0002-3586-3936>

Hao Hu  <https://orcid.org/0000-0003-3472-0404>

Jose Domingo Meza Aguilar  <https://orcid.org/0009-0004-9412-0413>



Madurangi E. Ranaweera  <https://orcid.org/0000-0001-6326-6226>  
 Michele A. Zacks  <https://orcid.org/0000-0003-4277-7689>  
 Julian J.-L. Chen  <https://orcid.org/0000-0002-7253-2722>  
 Debra T. Hansen  <https://orcid.org/0000-0003-4395-8297>  
 Lynn G. Schrag  <https://orcid.org/0000-0002-7704-8841>  
 Raimund Fromme  <https://orcid.org/0000-0003-4835-1080>  
 Sabine Botha  <https://orcid.org/0000-0003-4362-7543>  
 Petra Fromme  <https://orcid.org/0000-0003-0953-4909>

## REFERENCES

- Afonine PV, Grosse-Kunstleve RW, Echols N, Headd JJ, Moriarty NW, Mustyakimov M, et al. Towards automated crystallographic structure refinement with phenix.refine. *Acta Cryst D Struct Biol*. 2012;68:352–67.
- Agirre J, Atanasova M, Bagdonas H, Ballard CB, Baslé A, Beilstein-Edmonds J, et al. The CCP4 suite: integrative software for macromolecular crystallography. *Acta Crystallogr D Struct Biol*. 2023;79:449–61.
- Bhardwaj K, Palaninathan S, Alcantara JMO, Li Yi L, Guarino L, Sacchettini JC, et al. Structural and functional analyses of the severe acute respiratory syndrome coronavirus endoribonuclease Nsp15. *J Biol Chem*. 2008;283:3655–64.
- Bhardwaj K, Sun J, Holzenburg A, Guarino LA, Kao CC. RNA recognition and cleavage by the SARS coronavirus endoribonuclease. *J Mol Biol*. 2006;361:243–56.
- Brehm W, Diederichs K. Breaking the indexing ambiguity in serial crystallography. *Acta Crystallogr D Biol Crystallogr*. 2014;70:101–9.
- CDC. SARS-CoV-2 Variant Classifications and Definitions. 2023.
- Choi R, Zhou M, Shek R, Wilson JW, Tillery L, Craig JK, et al. High-throughput screening of the ReFRAME, pandemic box, and COVID box drug repurposing libraries against SARS-CoV-2 nsp15 endoribonuclease to identify small-molecule inhibitors of viral activity. *PLoS One*. 2021;16:e0250019.
- Doak RB, Shoeman RL, Gorel A, Niziński S, Barends TRM, Schlichting I. Sheet-on-sheet fixed target data collection devices for serial crystallography at synchrotron and XFEL sources. *J Appl Cryst*. 2024;57:1725–32.
- Duisenberg AJM. Indexing in single-crystal diffractometry with an obstinate list of reflections. *J Appl Cryst*. 1992;25:92–6.
- Emsley P, Lohkamp B, Scott WG, Cowtan K. Features and development of Coot. *Acta Crystallogr D Biol Crystallogr*. 2010;66:486–501.
- Evans PR, Murshudov GN. How good are my data and what is the resolution? *Acta Crystallogr Sect D Biol Crystallogr*. 2013;69(7):1204–14. <https://doi.org/10.1107/S0907444913000061>
- Frazier MN, Dillard LB, Krahn JM, Perera L, Williams JG, Wilson IM, et al. Characterization of SARS2 Nsp15 nuclease activity reveals it's mad about U. *Nucleic Acids Res*. 2021;49:10136–49.
- Frazier MN, Wilson IM, Krahn JM, Butay KJ, Dillard LB, Borgnia MJ, et al. Flipped over U: structural basis for dsRNA cleavage by the SARS-CoV-2 endoribonuclease. 2022a. *bioRxiv* [preprint].
- Frazier MN, Wilson IM, Krahn JM, Butay KJ, Dillard LB, Borgnia MJ, et al. Flipped over U: structural basis for dsRNA cleavage by the SARS-CoV-2 endoribonuclease. *Nucleic Acids Res*. 2022b;50:8290–301.
- Galanopoulos M, Doukatas A, Gazouli M. Origin and genomic characteristics of SARS-CoV-2 and its interaction with angiotensin converting enzyme type 2 receptors, focusing on the gastrointestinal tract. *World J Gastroenterol*. 2020;26:6335–45.
- Gevorkov Y, Yefanov O, Barty A, White TA, Mariani V, Brehm W, et al. XGANDALF—Extended gradient descent algorithm for lattice finding. *Acta Crystallogr A Found Adv*. 2019;75:694–704.
- Ginn HM, Roedig P, Kuo A, Evans G, Sauter NK, Ernst OP, et al. TakeTwo: an indexing algorithm suited to still images with known crystal parameters. *Acta Crystallogr D Struct Biol*. 2016;72:956–65.
- Guarino LA, Bhardwaj K, Dong W, Sun J, Holzenburg A, Kao C. Mutational analysis of the SARS virus Nsp15 endoribonuclease: identification of residues affecting hexamer formation. *J Mol Biol*. 2005;353(5):1106–17.
- Hackbart M, Deng X, Baker SC. Coronavirus endoribonuclease targets viral polyuridine sequences to evade activating host sensors. *Proc Natl Acad Sci U S A*. 2020;117:8094–103.
- Ito F, Yang H, Zhou ZH, Chen XS. Structural basis for polyuridine tract recognition by SARS-CoV-2 Nsp15. *Protein Cell*. 2024;15:547–52.
- Jernigan RJ, Logeswaran D, Doppler D, Nagaratnam N, Sonker M, Yang JH, et al. Room-temperature structural studies of SARS-CoV-2 protein NendoU with an X-ray free-electron laser. *Structure*. 2023;31:138–151.e5.
- Joosten RP, Long F, Murshudov GN, Perrakis A. The PDB\_REDO server for macromolecular structure model optimization. *IUCrJ*. 2014;1:213–20.
- Kabsch W. Xds. *Acta Crystallogr D Biol Crystallogr*. 2010;66:125–32.
- Kim D, Lee JY, Yang JS, Kim JW, Kim VN, Chang H. The architecture of SARS-CoV-2 transcriptome. *Cell*. 2020a;181:914–921.e10.
- Kim Y, Jedrzejczak R, Maltseva NI, Wilamowski M, Endres M, Godzik A, et al. Crystal structure of Nsp15 endoribonuclease NendoU from SARS-CoV-2. *Protein Sci*. 2020b;29:1596–605.
- Kim Y, Wower J, Maltseva N, Chang C, Jedrzejczak R, Wilamowski M, et al. Tipiracil binds to uridine site and inhibits Nsp15 endoribonuclease NendoU from SARS-CoV-2. *Commun Biol*. 2021;4:193.
- Machhi J, Herskovitz J, Senan AM, Dutta D, Nath B, Oleynikov MD, et al. The natural history, pathobiology, and clinical manifestations of SARS-CoV-2 infections. *J Neuroimmune Pharmacol*. 2020;15:359–86.
- Murshudov GN, Skubak P, Lebedev AA, Pannu NS, Steiner RA, Nicholls RA, et al. REFMAC5 for the refinement of macromolecular crystal structures. *Acta Crystallogr D Biol Crystallogr*. 2011;67:355–67.
- Orlans J, Ferguson G, Oscarsson M, Homs Puron A, Beteva A, Debionne S, et al. Advancing macromolecular structure determination with microsecond X-ray pulses at a 4th generation synchrotron. *Commun Chem*. 2025;8(1):6. <https://doi.org/10.1038/s42004-024-01404-y>
- Otter CJ, Bracci N, Parenti NA, Ye C, Asthana A, Blomqvist EK, et al. SARS-CoV-2 nsp15 endoribonuclease antagonizes dsRNA-induced antiviral signaling. *Proc Natl Acad Sci U S A*. 2024;121:e2320194121.
- Pillon MC, Frazier MN, Dillard LB, Williams JG, Kocaman S, Krahn JM, et al. Cryo-EM structures of the SARS-CoV-2 endoribonuclease Nsp15 reveal insight into nuclease specificity and dynamics. *Nat Commun*. 2021;12:636.
- Powell HR. The Rossmann Fourier autoindexing algorithm in MOSFLM. *Acta Crystallogr D Biol Crystallogr*. 1999;55:1690–5.
- Schrodinger, LLC. The PyMOL Molecular Graphics System, Version 2.0. 2015.
- Shu Y, McCauley J. GISAID: Global initiative on sharing all influenza data—from vision to reality. *Euro Surveill*. 2017;22:30494.
- Stefano Ricagno M-PE, Ulferts R, Coutard B, Nurizzo D, Campanacci V, Cambillau C, et al. Crystal structure and mechanistic determinants of SARS coronavirus nonstructural protein 15 define an endoribonuclease family. *PNAS*. 2006;103:11892–7.



- Vagin A, Teplyakov A. MOLREP: an automated program for molecular replacement. *J Appl Cryst*. 1997;30:1022–5.
- van Beusekom B, Touw WG, Tatineni M, Somani S, Rajagopal G, Luo J, et al. Homology-based hydrogen bond information improves crystallographic structures in the PDB. *Protein Sci*. 2018;27:798–808.
- van Loy B, Stevaert A, Naesens L. The coronavirus nsp15 endoribonuclease: a puzzling protein and pertinent antiviral drug target. *Antiviral Res*. 2024;228:105921.
- White TA. Processing serial crystallography data with CrystFEL: a step-by-step guide. *Acta Crystallogr D Struct Biol*. 2019;75:219–33.
- White TA, Kirian RA, Martin AV, Aquila A, Nass K, Barty A, et al. CrystFEL: a software suite for snapshot serial crystallography. *J Appl Cryst*. 2012;45:335–41.
- Wilson IM, Frazier MN, Li JL, Randall TA, Stanley RE. Biochemical characterization of emerging SARS-CoV-2 Nsp15 endoribonuclease variants. *J Mol Biol*. 2022;434:167796.
- Wu F, Zhao S, Yu B, Chen YM, Wang W, Song ZG, et al. A new coronavirus associated with human respiratory disease in China. *Nature*. 2020;579:265–9.
- Xu X, Zhai Y, Sun F, Lou Z, Su D, Xu Y, et al. New antiviral target revealed by the hexameric structure of mouse hepatitis virus nonstructural protein Nsp15. *J Virol*. 2006;80:7909–17.
- Zhang L, Li L, Yan L, Ming Z, Jia Z, Lou Z, et al. Structural and biochemical characterization of endoribonuclease Nsp15 encoded by Middle East respiratory syndrome coronavirus. *J Virol*. 2018;92:e00893-18.
- Zhang W, Davis BD, Chen SS, Sincuir Martinez JM, Plummer JT, Vail E. Emergence of a novel SARS-CoV-2 variant in Southern California. *JAMA*. 2021;325:1324–6.

## SUPPORTING INFORMATION

Additional supporting information can be found online in the Supporting Information section at the end of this article.

**How to cite this article:** Sonowal M, Ketawala G, Nagaratnam N, Logeswaran D, Basu S, de Sanctis D, et al. Functional implications of hexameric dynamics in SARS-CoV-2 Nsp15. *Protein Science*. 2025; 34(6):e70115. <https://doi.org/10.1002/pro.70115>